

## Plasmon-Driven Hot Electron Transfer at Atomically Sharp Metal–Semiconductor Nanojunctions

Masiar Sistani, Maximilian G. Bartmann, Nicholas A. Gsken, Rupert F. Oulton, Hamid Keshmiri, Minh Anh Luong, Zahra Sadre Momtaz, Martien I. Den Hertog, and Alois Lugstein\*

Cite This: *ACS Photonics* 2020, 7, 1642–1648

Read Online

ACCESS |

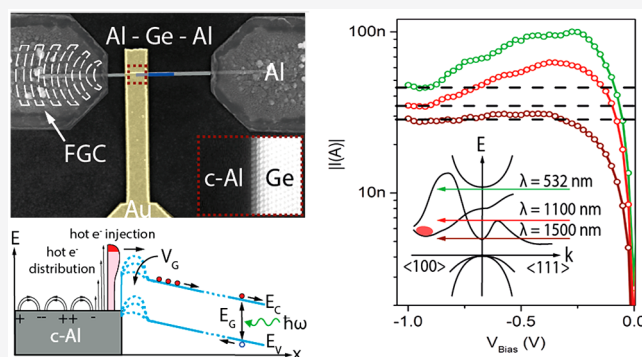
Metrics &amp; More

Article Recommendations

Supporting Information

**ABSTRACT:** Recent advances in guiding and localizing light at the nanoscale exposed the enormous potential of ultrascaled plasmonic devices. In this context, the decay of surface plasmons to hot carriers triggers a variety of applications in boosting the efficiency of energy-harvesting, photocatalysis, and photodetection. However, a detailed understanding of plasmonic hot carrier generation and, particularly, the transfer at metal–semiconductor interfaces is still elusive. In this paper, we introduce a monolithic metal–semiconductor (Al–Ge) heterostructure device, providing a platform to examine surface plasmon decay and hot electron transfer at an atomically sharp Schottky nanojunction. The gated metal–semiconductor heterojunction device features electrostatic control of the Schottky barrier height at the Al–Ge interface, enabling hot electron filtering. The ability of momentum matching and to control the energy distribution of plasmon-driven hot electron injection is demonstrated by controlling the interband electron transfer in Ge, leading to negative differential resistance.

**KEYWORDS:** surface plasmon, hot electrons, aluminum, germanium, nanowire, negative differential resistance



Plasmonic–metal nanostructures have become a powerful tool to concentrate and manipulate light below the diffraction limit, paving a pathway to couple optical energy effectively to nanoscale systems.<sup>1–4</sup> The plasmonic manipulation of light in metal–semiconductor (M–S) heterostructures became of particular interest due to their capability of generating hot electrons in the metal that can be transferred to the semiconductor and facilitate chemical reactions.<sup>5</sup> The selection of momentum-matched materials<sup>6</sup> and the design of optimized device architectures are thereby important for controlling plasmon-induced optical field distribution,<sup>7</sup> hot electron injection,<sup>8</sup> and energy transfer at a M–S heterojunction.<sup>9</sup> Propagating surface plasmons approaching a M–S interface can decay either radiatively<sup>10</sup> via scattering of photons or nonradiatively through the generation of hot carriers.<sup>11</sup> For radiative decay, photons are scattered from the metal into the adjacent semiconductor, driving electron–hole pair generation, commonly denoted internal photogeneration.<sup>12–16</sup> However, this mechanism is limited to energies above the semiconductor band gap,<sup>7</sup> and for Ge due to the indirect bandgap, the small electron–photon cross-section makes this process inherently inefficient.<sup>17</sup> For nonradiative plasmon decay, plasmon-driven electrons that simultaneously move toward the planar interface while also having sufficient kinetic energy to overcome the Schottky barrier may be directly injected into the semiconductor.<sup>17</sup> These injected hot

electrons exhibit a rather broad energy distribution, which stems from the almost continuous density of electronic energy states that exist below the Fermi level of metals.<sup>15</sup> However, assuming excitation of electrons at the Fermi level, the maximum energy of the injected hot electrons is  $E = \hbar\omega_{\text{SPP}}$ ,<sup>7,17,18</sup> with  $\omega_{\text{SPP}}$  being the surface plasmon polariton (SPP) angular frequency.<sup>8</sup> Injection efficiencies less than 1% are expected due to a range of limiting processes, including ultrafast carrier–carrier relaxation,<sup>5</sup> the lack of vertical momentum of hot electrons, and reflection at the M–S interface.<sup>19</sup> Contributing to applications such as plasmon enhanced photocatalysis,<sup>5</sup> light harvesting<sup>9</sup> and photodetection,<sup>11</sup> we extend the vast body of pioneering work on experimental investigations on plasmon decay to hot electrons<sup>7,17,20–22</sup> by introducing a gated metal–semiconductor heterojunction device featuring electrostatic control of the Schottky barrier height at the Al–Ge interface, enabling hot electron filtering.

Received: April 7, 2020

Published: June 30, 2020



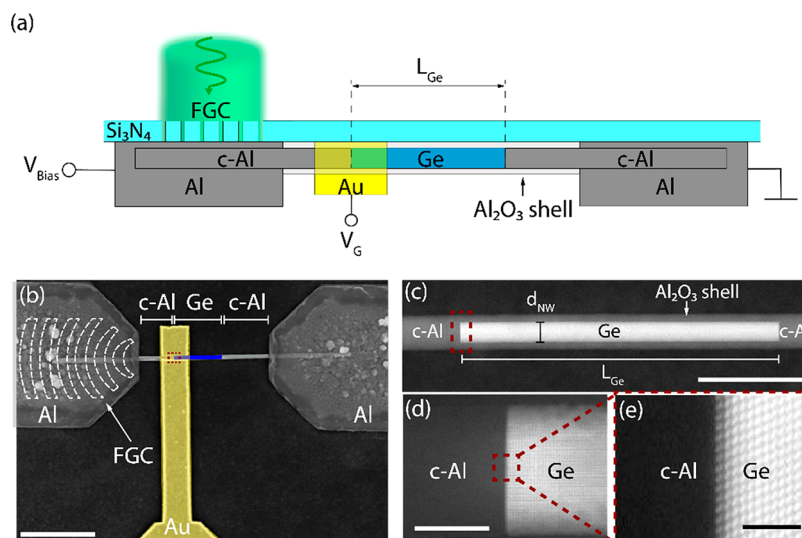


**Figure 1.** (a) Schematic illustration of the top-gated Al–Ge NW heterostructure device fabricated on a 40 nm thin  $\text{Si}_3\text{N}_4$  membrane. (b) False color SEM image of the GPTD device. The FGC atop of the  $\text{Si}_3\text{N}_4$  membrane is schematically indicated with dashed lines. Scale bar is 1  $\mu\text{m}$ . (c) HAADF STEM image of the entire Al–Ge–Al NW heterostructure comprising a Ge segment length of  $L_{\text{Ge}} = 600$  nm and a diameter of  $d_{\text{NW}} = 40$  nm wrapped by a 20 nm thick  $\text{Al}_2\text{O}_3$  shell. Scale bar is 200 nm. TEM images showing (d) the entire Al–Ge interface of the NW heterostructure (scale bar is 40 nm) and a zoomed-in image, where the Ge region is oriented on the  $[110]$  zone axis (scale bar is 5 nm).

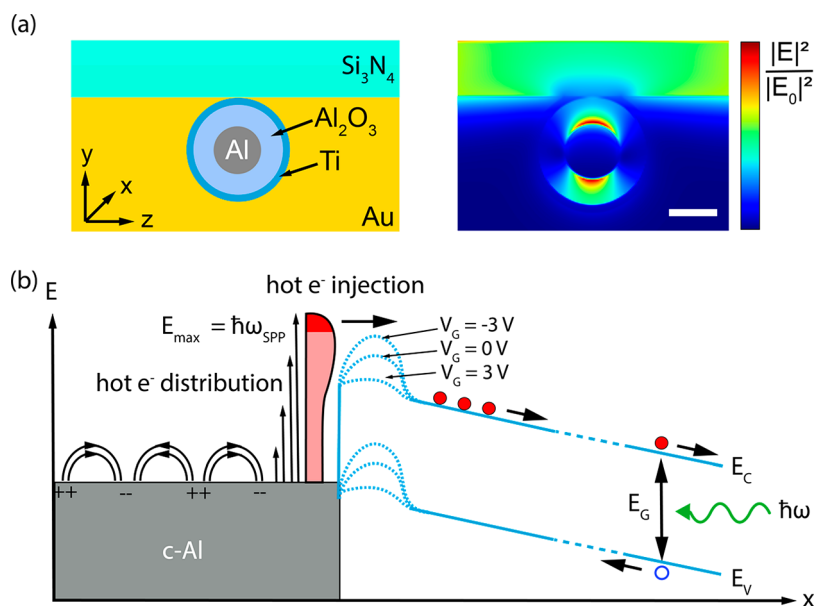


**Figure 2.** (a) Illustration of the gated c-Al NW segment cross section in the vicinity of the Al–Ge nanojunction indicating the different material layers surrounding the NW. The according simulated distribution of the normalized electric field intensity ( $|E|^2/|E_0|^2$ ) in direct vicinity to the Al–Ge interface of the fundamental mode is shown on the right. The individual field contributions  $|E_x|^2$ ,  $|E_y|^2$ ,  $|E_z|^2$  are illustrated in Figure S2. Here, coupling of TM polarized light via the FGC ( $\lambda = 532$  nm) is considered. The simulations show that the mode is bound to the c-Al NW even underneath the gate. The scale bar is 40 nm. (b) Schematic illustration of SPP propagation along the c-Al NW, SPP decay induced carrier injection into the Ge segment and the band-diagram with gate dependent barrier height. The green arrow schematically shows photoexcitation of the Ge segment and the associated electron–hole pair generation.

## RESULTS AND DISCUSSION

In this work, we investigate surface plasmon-driven electron transfer processes at an atomically sharp M–S nanojunction of a monolithic Al–Ge nanowire (NW) heterostructure. Figure 1a,b shows the schematic and a false-color scanning electron microscopy (SEM) image of the gated plasmon transfer device (GPTD) comprising a focused grating coupler (FGC) to launch SPPs in the single crystalline Al (c-Al) NW plasmon waveguide attached to the semiconducting Ge segment. An

omega-shaped gate electrode directly atop of the atomically sharp heterojunction enables electrostatic control of the Schottky barrier at the M–S interface.<sup>24</sup> The device is realized on a 40 nm thick  $\text{Si}_3\text{N}_4$  membrane<sup>25</sup> by a thermally induced exchange reaction between single-crystalline Ge NWs covered by a passivating  $\text{Al}_2\text{O}_3$  shell and lithographically defined Al contact pads resulting in crystalline Al–Ge–Al NW heterostructures. More details regarding the Al–Ge heterostructure formation are described in the work of Kral et al.<sup>26</sup> and El Hajraoui et al.<sup>27</sup> The high angle annular dark field (HAADF)

scanning transmission electron microscopy (STEM) images in Figure 1c–e show the monolithic Al–Ge–Al nanowire heterostructure with atomically sharp interfaces enwrapped by a 20 nm thick passivating Al<sub>2</sub>O<sub>3</sub> shell.

Effective surface plasmon excitation is achieved by coupling normal incident TM polarized laser with a vacuum wavelength of  $\lambda = 532$  nm into the c-Al NW waveguide using a Si<sub>3</sub>N<sub>4</sub> membrane FGC,<sup>28</sup> located above the Al contact pad (see Figure 1a,b).<sup>29</sup> As previously shown, for such a configuration, we experimentally determined a SPP propagation length of  $L_{\text{SPP}} = 140$  nm at  $\lambda = 532$  nm for 40 nm thin c-Al NWs.<sup>29</sup> With respect to the actual device geometry, Finite Difference Time Domain (FDTD) simulations revealed that adding the omega-shaped gate atop the Al–Ge nanojunction significantly lowers the LSPP (see Figure S1).

Figure 2a shows a cross-sectional schematic of the Al plasmonic waveguide enwrapped by the Al<sub>2</sub>O<sub>3</sub> shell and the omega-shaped metal gate. FDTD simulations confirm a bound mode propagation along the NW, underneath the gate and right until the Al–Ge interface. Here, the entire propagation pathway of a TM polarized incident beam coupled via the FGC to the c-Al-NW and the gated Al–Ge NW junction was considered. Figure 2a shows the field intensity distribution of the coupled light in close vicinity to the gated Al–Ge interface where hot carriers are excited. The individual field intensity distributions  $|E_x|^2$ ,  $|E_y|^2$ ,  $|E_z|^2$  are shown in Figure S2. Additional field intensity distributions at  $\lambda = 1100$ , 1500, and 1800 nm are illustrated in Figure S3 for comparison. Further, Figure S4 shows a field intensity cross-section of the gated Al–Ge nanojunction in the  $xz$ -plane for an excitation of  $\lambda = 1100$  nm. The simulation shows clearly the feasibility of plasmon guiding underneath the gate electrode and plasmon decay at the Al–Ge interface.

The omega-shaped top gate at the M–S interface enables tuning of the Schottky barrier height at the M–S heterojunction. In fact, the electrical characteristic of the heterojunction can be tuned between Ohmic and Schottky behaviors (Figure S5). According to the schematic in Figure 2b, only hot electrons that move toward the nanojunction with sufficiently high energies overcome the barrier and enter the Ge segment, following nonradiative SPP decay. According to the work of Sundararaman et al.,<sup>7</sup> we assumed a continuous hot electron energy distribution reaching from the Fermi level of Al to the maximum energy  $E = \hbar\omega_{\text{SPP}}$  (see schematic in Figure 2b). By applying a bias voltage ( $V_{\text{Bias}}$ ), as shown in Figure 1a, for a given barrier height, these injected charge carriers induce a current, further denoted as SP-current. Thus, with the GPTD, we can detect surface plasmons by direct electrical means<sup>23,30</sup> and even tune the energy of the electrons surpassing the Schottky junction of this M–S plasmon detector.

To demonstrate the mode of operation of the electrostatically tunable barrier, which works as an energetic filter for plasmon-driven hot electron injection, we performed wavelength dependent measurements. A tunable laser was focused on the FGC and the plasmon-driven hot electron transfer was investigated measuring the SP-current through the GPTD as a function of the gate potential. Figure 3 shows a comparison of the SP-current (red) with the photocurrent (PH-current) induced by directly focusing the laser onto the Ge segment (blue dotted curves). A PH-current only occurs for photon energies slightly higher than the direct bandgap ( $E_{\text{Ti}}$ ) and appeared to be independent of the gate voltage. A SP-current occurs for both interband excitation as well as plasmon-driven

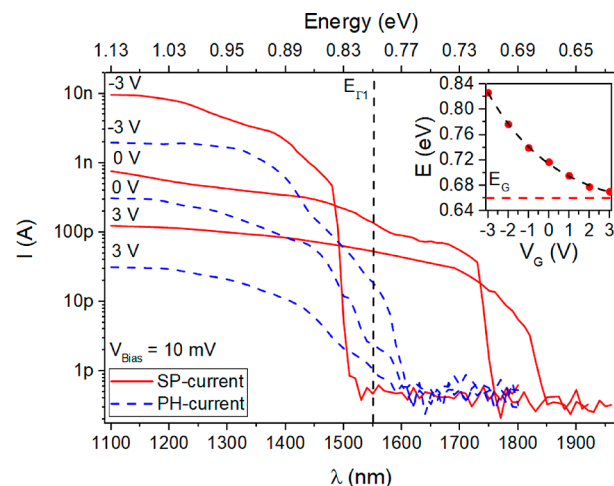


**Figure 3.** Spectral response of the SP- and PH-current for a bias voltage of  $V_{\text{Bias}} = 10$  mV and gate voltages between  $-3$  and  $3$  V. The inset shows the thereof evaluated energy of hot electrons extracted from wavelength-dependent measurements of the SP-current.

hot electron injection, which is tunable by the gate voltage (within the physical limit of the gate dielectric) from about 1500 nm to about 1850 nm. For increasing gate voltage, corresponding to a lowering of the Schottky barrier height, less energetic electrons can surpass the junction and contribute to the SP-current, even when the photon energy coupled into the c-Al waveguides is below the direct bandgap energy of Ge (0.8 eV). This sub-bandgap photodetection rules out a mechanism based upon direct photogeneration at the M–S interface.

Assuming that the plasmon-induced near field drives the hot electron generation,<sup>7,17</sup> the maximum wavelength where SP-current can still be measured for a certain gate voltage, indicates both the maximum energy of injected electrons into the Ge as well as the Schottky barrier height. Thus, the inset in Figure 3 shows the calculated effective barrier heights for plasmon-driven hot electron transfer from the c-Al waveguide into the Ge detector as a function of the gate voltage. The thereof, estimated injection efficiencies according to Fowler's theory<sup>31</sup> for gate voltages of  $V_G = -3, 0,$  and  $3$  V are plotted in Figure S6. We want to note that this estimation is not considering a range of limiting processes, including ultrafast carrier–carrier relaxation,<sup>5</sup> the lack of vertical momentum of hot electrons, and reflection at the M–S interface.<sup>19</sup>

The ability to control the energy and momentum of plasmon-driven hot electrons injected into the Ge enables us to induce negative differential resistance (NDR),<sup>32</sup> an effect that may be used for fast switching logic circuits, static memory cells, or high-frequency oscillators.<sup>33</sup> NDR can arise from electrons with sufficiently high energy being scattered to a heavy mass valley with a lower mobility, thus, increasing the resistivity of the Ge.<sup>34</sup> This so-called transferred electron effect has been observed at high electric fields in numerous systems, perhaps best known as the Gunn effect in GaAs,<sup>35</sup> but also GaN nanocrystals<sup>36</sup> and Ni/Ge Schottky diodes.<sup>37</sup>

To investigate such SPP momentum-induced NDR in Ge, the GPTD was operated as a Schottky barrier field effect transistor (FET). The black curve in the semilogarithmic plot of Figure 4 shows the  $I/V$  characteristic with the drain current  $I \propto \exp(eV/k_B T)$ , which is typical for semiconductor NW devices with two back-to-back Schottky contacts.<sup>38</sup> The rectifying behavior is a direct consequence of different barrier

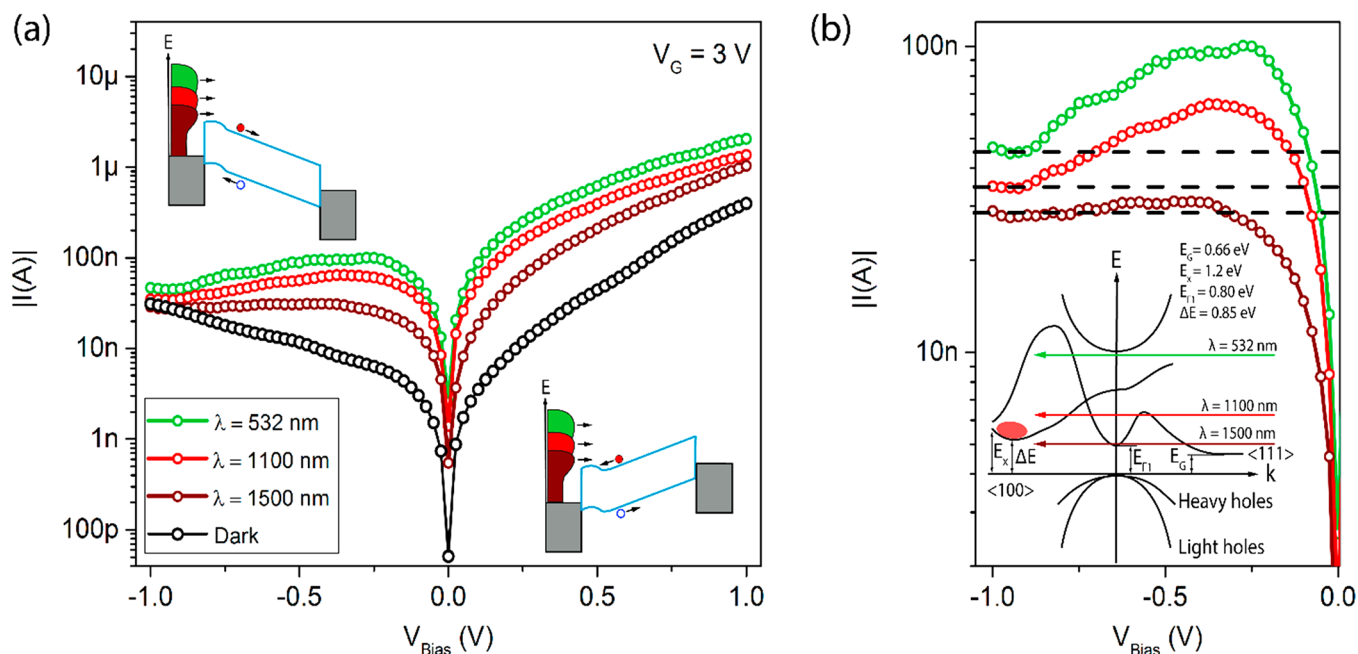


**Figure 4.** (a) Dark current and SP-current recorded for excitation wavelengths of  $\lambda = 532$ , 1100, and 1500 nm at  $V_G = 3$  V. The insets show the respective band diagrams for applying a positive and negative bias voltage to the heterostructure device. (b) Zoom showing the region of NDR. The inset shows the band diagram of Ge with the hot carrier injection into the  $\langle 100 \rangle$  valley indicated.

heights of the M-S junctions interfacing the NW.<sup>39–41</sup> The SP-currents with laser illumination at the FGC at  $\lambda = 532$ , 1100, and 1500 nm are shown in green, red, and dark red, respectively. For a gate voltage of 3 V and, thus, low Schottky barrier height, plasmon-driven hot electrons are effectively injected into the Ge segment, thus, inducing a large SP-current. At positive bias voltages we observed a steady SP-current increase for all three wavelengths. The injected hot electrons arising from the plasmon decay at the Al–Ge interface are moving against the electric field and undergo thermalization via electron–electron and electron–phonon scattering as well as electron–hole pair generation (see lower inset in Figure 4).<sup>42</sup> These additional charge carriers are swept out from the Ge segment driven by the electric field and contribute to the overall current through the FET. For negative bias, NDR is observed, with a maximum peak to valley ratio of 2.3 for the SP-current recorded for plasmon excitation with a laser wavelength of  $\lambda = 532$  nm (green curve). Note that for negative bias the plasmon-driven hot electrons are injected with a momentum aligned to the electrical field in the Ge segment and are thus accelerated (upper inset).

According to the Ridley-Watkins-Hilsum theory,<sup>37</sup> NDR via an electron transfer process requires the lower and upper valleys between which electrons are transferred to be separated by an energy difference much larger than the thermal energy but smaller than the energy gap of the semiconductor. This holds for Ge as the energy difference between the L-point and  $\Delta$ -point minima of the  $\langle 111 \rangle$  and  $\langle 100 \rangle$  sub-bands of  $\Delta E = 0.19$  eV<sup>38</sup> is significantly higher than the thermal energy at room temperature ( $k_B T = 25.8$  meV) but much less than the bandgap ( $E_G = 0.66$  eV; inset of Figure 4b).<sup>38</sup> To finally achieve NDR, it is required that electrons in the lower valley have a lower effective mass than those in the upper valley.<sup>35</sup> For Ge, the transverse effective electron mass in the  $\Delta$ -point,  $m_{\Delta,t}^* = 0.288m_0$ , is significantly higher than that in the L-point minimum,  $m_{L,t}^* = 0.082m_0$ .<sup>43</sup> Although the  $\Gamma$ -point minimum

is energetically closer to the L-point minimum, the coupling constant between the 111 and 000 minima is significantly lower than between the 111 and 100 minima.<sup>43</sup> Thus, the transfer of electrons mainly occurs from the L-valley to the  $\Delta$ -valley and the respective energy difference of  $\Delta E = 0.19$  eV<sup>38</sup> determines the threshold electric field for electron repopulation. Hot electrons arising from the plasmon decay at the Al–Ge interface are already at a higher energy level and require only moderate electric fields to overcome a smaller energy difference to be scattered to the  $\Delta$ -valley. Accordingly, the NDR effect fades out as the energy of the hot electrons declines for exciting the FGC with laser light at  $\lambda = 1500$  nm. Therefore, the maximum energy of injected hot electrons (0.82 eV) is not sufficient anymore to inject electrons effectively into the  $\Delta$ -valley.

It is important to note that our measurements provide substantial experimental evidence that the momentum of hot electrons originating from surface plasmon decay is suitable for scattering into the lower mobility  $\Delta$ -valley of Ge. In contrast, no signs of NDR could be found for directly focusing the laser onto the Ge segment (see Figure S7).

## CONCLUSIONS

In conclusion, we have demonstrated a near-field electrical SPP detector providing a platform to independently examine plasmon-induced hot carrier injection and photoexcitation. The system is based on a monolithic axial M-S-M heterostructure that features a precise control of the injection barrier height at an abrupt M-S interface, enabling the probing of the hot electron injection from SPP decay. This architecture allows an investigation of hot electron transport effects initiated by SPP decay at an atomically sharp M-S heterojunction. By precisely controlling the injection barrier and SPP excitation, we demonstrated SPP momentum induced NDR. In contrast, no signs of NDR could be found for directly focusing the laser onto the Ge segment. Thus, the

demonstrated investigations provide a route to a better understanding of plasmonic hot electron devices and may pave the way for novel device concepts based on a plasmon-induced NDR.

## METHODS/EXPERIMENTAL DETAILS

**Device Fabrication.** The starting materials were VLS grown Ge NWs with diameters between 30 and 50 nm coated with 20 nm high- $k$   $\text{Al}_2\text{O}_3$  using atomic layer deposition. The Ge NWs were drop casted onto 40 nm thin  $\text{Si}_3\text{N}_4$  membranes<sup>25</sup> and contacted by Al pads fabricated by electron beam lithography, 100 nm Al sputter deposition and lift-off techniques. A successive thermally induced exchange reaction by rapid thermal annealing at a temperature of  $T = 624$  K in forming gas atmosphere initiates the substitution of the Ge core by c-Al.<sup>26,27</sup> An omega-shaped Ti/Au top-gate was fabricated above the M-S interface using electron beam lithography, Ti/Au electron-beam evaporation (8 nm Ti, 100 nm Au), and lift-off techniques. To complete the device, the FIB column of a Zeiss Neon 40EsB CrossBeam system was used to pattern the FGC in the  $\text{Si}_3\text{N}_4$  membranes. The milling current was set to 50 pA.

**High-Resolution HAADF STEM.** HAADF STEM was performed on Al–Ge–Al NW heterostructures fabricated on 40 nm thick  $\text{Si}_3\text{N}_4$  membranes<sup>25</sup> using a probe-corrected FEI Titan Themis, working at 200 kV. The Al–Ge interface in the shown images was oriented along the [110] direction of observation of the Ge crystal.

**Electrical and Optical Characterization.** The biasing of the proposed Al–Ge–Al NW heterostructures was performed using a Keysight B1500A semiconductor analyzer. For optical excitation, a frequency doubled Nd:YAG laser emitting linearly polarized light at  $\lambda = 532$  nm was coupled into a WITec Alpha300 and focused on the device through a Zeiss 100 $\times$  objective (NA = 0.75, WD = 4 mm), enabling a diffraction limited spot size of  $\sim 865$  nm. The output power of the system was set to have negligible laser heating effects in the NW. For investigating the spectral response of the plasmon current, the white light from a broadband laser source (SuperK Extreme, NKT) fiber was coupled to a monochromator (SuperK Select, NKT). The output of this system is supplied to a NKT SuperK Select acoustic-optical tunable filter (AOTF). The system consists of three AOTFs, which act as monochromators with separated channels for visible ( $\lambda = 500$ –700 nm), near-infrared ( $\lambda = 600$ –1100 nm), and infrared ( $\lambda = 1100$ –2000 nm) light. The output from the AOTFs is coupled into a WITec Alpha300. The beam is passing a 50–50 beam splitter and is focused on the sample through a Zeiss 100 $\times$  objective (NA = 0.75, WD = 4 mm). The output is focused on the device with power densities chosen to have negligible laser heating effects in the NW.

**FDTD Simulations.** Numerical 3D FDTD calculations were performed using commercial software (Lumerical). The entire 3D system, including the incoupling FGC and the Al–Ge–Al NW heterostructure, were considered. A Gaussian beam served as source with a central wavelength of  $\lambda = 532$  nm, illuminating the FGC. The mesh size was set to 0.4 nm, allowing to account for the minimum feature sizes of the structure. The electric field intensities indicated are normalized by the source intensity value  $|E_0|^2$ .

## ASSOCIATED CONTENT

### Supporting Information

The Supporting Information is available free of charge at <https://pubs.acs.org/doi/10.1021/acsphotonics.0c00557>.

*Calculation of the SPP propagation length as a function of the exciting wavelength at the FGC, simulated distributions of the normalized electric field intensity at the Al–Ge interface, simulated field intensity horizontal cross-section of the gated Al–Ge nanojunction in the  $xz$ -plane for an excitation with  $\lambda = 1100$  nm at the FGC,  $I/V$  measurements showing the ability to tune the Ge detector from an Ohmic behavior to a Schottky behavior and PH-current measurement at  $V_G = 3$  V, calculated injection efficiency of hot electrons through the Al–Ge interface according to Fowler's theory (PDF)*

## AUTHOR INFORMATION

### Corresponding Author

Alois Lugstein – Institute of Solid State Electronics, Technische Universität Wien, 1040 Vienna, Austria; [orcid.org/0000-0001-5693-4775](https://orcid.org/0000-0001-5693-4775); Email: [alouis.lugstein@tuwien.ac.at](mailto:alouis.lugstein@tuwien.ac.at)

### Authors

Masiar Sistani – Institute of Solid State Electronics, Technische Universität Wien, 1040 Vienna, Austria; [orcid.org/0000-0001-5730-234X](https://orcid.org/0000-0001-5730-234X)

Maximilian G. Bartmann – Institute of Solid State Electronics, Technische Universität Wien, 1040 Vienna, Austria

Nicholas A. Günsken – The Blackett Laboratory, Department of Physics, Imperial College London, London SW7 2AZ, United Kingdom; [orcid.org/0000-0002-4816-0666](https://orcid.org/0000-0002-4816-0666)

Rupert F. Oulton – The Blackett Laboratory, Department of Physics, Imperial College London, London SW7 2AZ, United Kingdom

Hamid Keshmiri – Institute of Solid State Electronics, Technische Universität Wien, 1040 Vienna, Austria

Minh Anh Luong – Univ. Grenoble Alpes, CEA, INAC, MEM, F-38000 Grenoble, France

Zahra Sadre Momtaz – Institut NEEL CNRS/UGA UPR2940, F-38042 Grenoble, France

Martien I. Den Hertog – Institut NEEL CNRS/UGA UPR2940, F-38042 Grenoble, France; [orcid.org/0000-0003-0781-9249](https://orcid.org/0000-0003-0781-9249)

Complete contact information is available at:

<https://pubs.acs.org/doi/10.1021/acsphotonics.0c00557>

### Author Contributions

M.S. and M.G.B. fabricated the devices and conducted the measurements. N.A.G. conducted the FDTD simulations describing the NW- $\text{Si}_3\text{N}_4$  membrane system. N.A.G. and R.F.O. contributed to the explanation of the underlying physical mechanisms. H.K. designed the FGC. Z.S.M. fabricated the  $\text{Si}_3\text{N}_4$  membranes and M.A.L. and M.I.H. carried out TEM characterization. A.L. conceived the project, contributed essentially to the experimental design and provided expertise on theoretical interpretations. The manuscript was written through contributions of all authors. All authors have given approval to the final version of the manuscript.

### Notes

The authors declare no competing financial interest.

## ACKNOWLEDGMENTS

The authors gratefully acknowledge financial support by the Austrian Science Fund (FWF): Project No. P29729–N27. The authors further thank the Center for Micro- and Nanostructures for providing the cleanroom facilities. We acknowledge support from the Laboratoire d'excellence LANEF in Grenoble (ANR-10-LABX-51-01). Financial support from the ANR-COSMOS (ANR-12-JS10-0002) project is acknowledged. We benefitted from the access to the Nano characterization platform (PFNC) in CEA Minatec Grenoble in collaboration with the LEMMA/IRIG group. We acknowledge support from Campus France in the framework of PHC AMADEUS 2016 for PROJET No. 35592PB. This project has received funding from the European Research Council (ERC) under the European Union's Horizon 2020 research and innovation program (Grant Agreement No. 758385) for the e-See Project.

## REFERENCES

- (1) Ozbay, E. Plasmonics: Merging Photonics and Electronics at Nanoscale Dimensions. *Science* **2006**, *311*, 189–193.
- (2) Atwater, H. A.; Polman, A. Plasmonics for Improved Photovoltaic Devices. *Nat. Mater.* **2010**, *9*, 205–213.
- (3) Wei, H.; Pan, D.; Zhang, S.; Li, Z.; Li, Q.; Liu, N.; Wang, W.; Xu, H. Plasmon Waveguiding in Nanowires. *Chem. Rev.* **2018**, *118*, 2882–2926.
- (4) Sorger, V. J.; Oulton, R. F.; Ma, R.-M.; Zhang, X. Toward Integrated Plasmonic Circuits. *MRS Bull.* **2012**, *37*, 728–738.
- (5) Narang, P.; Sundararaman, R.; Atwater, H. A. Plasmonic Hot Carrier Dynamics in Solid-State and Chemical Systems for Energy Conversion. *Nanophotonics* **2016**, *5*, 96–111.
- (6) Jia, C.; Lin, Z.; Huang, Y.; Duan, X. Nanowire Electronics: From Nanoscale to Macroscale. *Chem. Rev.* **2019**, *119*, 9074–9135.
- (7) Sundararaman, R.; Narang, P.; Jermyn, A. S.; Goddard, W. A., III; Atwater, H. A. Theoretical Predictions for Hot-Carrier Generation from Surface Plasmon Decay. *Nat. Commun.* **2014**, *5*, 5788.
- (8) Maier, S. A. *Plasmonics: Fundamentals and Applications*; Springer Science, 2007.
- (9) Wang, F.; Melosh, N. A. Plasmonic Energy Collection through Hot Carrier Extraction. *Nano Lett.* **2011**, *11*, 5426–5430.
- (10) Giannini, V.; Fernández-Domínguez, A. I.; Heck, S. C.; Maier, S. A. Plasmonic Nanoantennas: Fundamentals and Their Use in Controlling the Radiative Properties of Nanoemitters. *Chem. Rev.* **2011**, *111*, 3888–3912.
- (11) Brongersma, M. L. Plasmonic Photodetectors, Photovoltaics, and Hot-Electron Devices. *Proc. IEEE* **2016**, *104*, 2349–2361.
- (12) Goykhman, I.; Desiatov, B.; Khurgin, J.; Shappir, J.; Levy, U. Locally Oxidized Silicon Surface-Plasmon Schottky Detector for Telecom Regime. *Nano Lett.* **2011**, *11*, 2219–2224.
- (13) Muehlbrandt, S.; Melikyan, A.; Harter, T.; Köhnle, K.; Muslija, A.; Vincze, P.; Wolf, S.; Jakobs, P.; Fedoryshyn, Y.; Freude, W.; Leuthold, J.; Koos, C.; Kohl, M. Silicon-Plasmonic Internal-Photoemission Detector for 40 Gbit/s Data Reception. *Optica* **2016**, *3*, 741.
- (14) Akbari, A.; Berini, P. Schottky Contact Surface-Plasmon Detector Integrated with an Asymmetric Metal Stripe Waveguide. *Appl. Phys. Lett.* **2009**, *95*, 021104.
- (15) White, T. P.; Catchpole, K. R. Plasmon-Enhanced Internal Photoemission for Photovoltaics: Theoretical Efficiency Limits. *Appl. Phys. Lett.* **2012**, *101*, 073905.
- (16) Knight, M. W.; Sobhani, H.; Nordlander, P.; Halas, N. J. Photodetection with Active Optical Antennas. *Science* **2011**, *332*, 702–704.
- (17) Zheng, B. Y.; Zhao, H.; Manjavacas, A.; McClain, M.; Nordlander, P.; Halas, N. J. Distinguishing between Plasmon-Induced and Photoexcited Carriers in a Device Geometry. *Nat. Commun.* **2015**, *6*, 7797.
- (18) Clavero, C. Plasmon-Induced Hot-Electron Generation at Nanoparticle/Metal-Oxide Interfaces for Photovoltaic and Photocatalytic Devices. *Nat. Photonics* **2014**, *8*, 95–103.
- (19) Khurgin, J. B. Hot Carriers Generated by Plasmons: Where Are They Generated and Where Do They Go from There? *Faraday Discuss.* **2019**, *214*, 35–58.
- (20) Gundlach, K. H.; Kadlec, J. Interfacial Barrier Height Measurement from Voltage Dependence of the Photocurrent. *J. Appl. Phys.* **1975**, *46*, 5286–5287.
- (21) Afanas'ev, V. V.; Houssa, M.; Stesmans, A.; Heyns, M. M. Band Alignments in Metal-Oxide-Silicon Structures with Atomic-Layer Deposited Al<sub>2</sub>O<sub>3</sub> and ZrO<sub>2</sub>. *J. Appl. Phys.* **2002**, *91*, 3079–3084.
- (22) Wang, F.; Melosh, N. A. Plasmonic Energy Collection through Hot Carrier Extraction. *Nano Lett.* **2011**, *11*, 5426–5430.
- (23) Govorov, A. O.; Zhang, H.; Gun'ko, Y. K. Theory of Photoinjection of Hot Plasmonic Carriers from Metal Nanostructures into Semiconductors and Surface Molecules. *J. Phys. Chem. C* **2013**, *117*, 16616–16631.
- (24) Yang, F.-L.; Chen, H.-Y.; Chen, F.-C.; Huang, C.-C.; Chang, C.-Y.; Chiu, H.-K.; Lee, C.-C.; Chen, C.-C.; Huang, H.-T.; Chen, C.-J.; Tao, H.-J.; Yeo, Y.-C.; Liang, M.-S.; Hu, C. 25 nm CMOS Omega FETs. *Digest. International Electron Devices Meeting*, San Francisco, CA, Dec 8–11, 2002, IEEE, 2002; pp 255–258.
- (25) den Hertog, M. I.; González-Posada, F.; Songmuang, R.; Rouviere, J. L.; Fournier, T.; Fernandez, B.; Monroy, E. Correlation of Polarity and Crystal Structure with Optoelectronic and Transport Properties of GaN/AlN/GaN Nanowire Sensors. *Nano Lett.* **2012**, *12*, 5691–5696.
- (26) Kral, S.; Zeiner, C.; Stöger-Pollach, M.; Bertagnolli, E.; den Hertog, M. I.; Lopez-Haro, M.; Robin, E.; El Hajraoui, K.; Lugstein, A. Abrupt Schottky Junctions in Al/Ge Nanowire Heterostructures. *Nano Lett.* **2015**, *15*, 4783–4787.
- (27) El Hajraoui, K.; Luong, M. A.; Robin, E.; Brunbauer, F.; Zeiner, C.; Lugstein, A.; Gentile, P.; Rouvière, J.-L.; Den Hertog, M. In Situ Transmission Electron Microscopy Analysis of Aluminum-Germanium Nanowire Solid-State Reaction. *Nano Lett.* **2019**, *19*, 2897–2904.
- (28) den Hertog, M.; Donatini, F.; McLeod, R.; Monroy, E.; Sartel, C.; Sallet, V.; Pernot, J. In Situ Biasing and Off-Axis Electron Holography of a ZnO Nanowire. *Nanotechnology* **2018**, *29*, 025710.
- (29) Sistani, M.; Bartmann, M. G.; Guskens, N. A.; Oulton, R. F.; Keshmiri, H.; Seifner, M. S.; Barth, S.; Fukata, N.; Luong, M. A.; den Hertog, M. I.; Lugstein, A. Nanoscale Aluminum Plasmonic Waveguide with Monolithically Integrated Germanium Detector. *Appl. Phys. Lett.* **2019**, *115*, 161107.
- (30) Falk, A. L.; Koppens, F. H. L.; Yu, C. L.; Kang, K.; de Leon Snapp, N.; Akimov, A. V.; Jo, M.-H.; Lukin, M. D.; Park, H. Near-Field Electrical Detection of Optical Plasmons and Single-Plasmon Sources. *Nat. Phys.* **2009**, *5*, 475–479.
- (31) Blandre, E.; Jalas, D.; Petrov, A. Y.; Eich, M. Limit of Efficiency of Generation of Hot Electrons in Metals and Their Injection inside a Semiconductor Using a Semiclassical Approach. *ACS Photonics* **2018**, *5*, 3613–3620.
- (32) Brunbauer, F. M.; Bertagnolli, E.; Lugstein, A. Gate-Tunable Electron Transport Phenomena in Al-Ge<<111>>-Al Nanowire Heterostructures. *Nano Lett.* **2015**, *15*, 7514–7518.
- (33) Berger, P. R.; Ramesh, A. *Negative Differential Resistance Devices and Circuits*; Elsevier, 2011.
- (34) Husain, M. K.; Li, X. V.; de Groot, C. H. Observation of Negative Differential Conductance in a Reverse-Biased Ni/Ge Schottky Diode. *IEEE Electron Device Lett.* **2009**, *30*, 966–968.
- (35) Butcher, P. N. The Gunn Effect. *Rep. Prog. Phys.* **1967**, *30*, 97.
- (36) Chitara, B.; Ivan Jebakumar, D. S.; Rao, C. N. R.; Krupanidhi, S. B. Negative Differential Resistance in GaN Nanocrystals above Room Temperature. *Nanotechnology* **2009**, *20*, 405205.
- (37) Ridley, B. K.; Watkins, T. B. The Possibility of Negative Resistance Effects in Semiconductors. *Proc. Phys. Soc., London* **1961**, *78*, 293–304.

(38) Ioffe Institute. Germanium band structure and carrier concentration, <http://www.ioffe.ru/SVA/NSM/Semicond/Ge/bandstr.html> (accessed March 3, 2020).

(39) Kumar Bhaskar, U.; Pardoen, T.; Passi, V.; Raskin, J.-P. Surface States and Conductivity of Silicon Nano-Wires. *J. Appl. Phys.* **2013**, *113*, 134502.

(40) Taur, Y.; Ning, T. H. *Fundamentals of Modern VLSI Devices*. Cambridge Univ. Press, 2013; p 310.

(41) Lee, S.-K.; Lee, S.-Y.; Rogdakis, K.; Jang, C.-O.; Kim, D.-J.; Bano, E.; Zekentes, K. Si Nanowire P-FET with Asymmetric Source-Drain Characteristics. *Solid State Commun.* **2009**, *149*, 461–463.

(42) Chalabi, H.; Brongersma, M. L. Harvest Season for Hot Electrons. *Nat. Nanotechnol.* **2013**, *8*, 229–230.

(43) Jacoboni, C.; Nava, F.; Canali, C.; Ottaviani, G. Electron Drift Velocity and Diffusivity in Germanium. *Phys. Rev. B: Condens. Matter Mater. Phys.* **1981**, *24*, 1014–1026.